Scripta Materialia 204 (2021) 114133

Contents lists available at ScienceDirect

Scripta Materialia

journal homepage: www.elsevier.com/locate/scriptamat

Stabilizing voltage and prolonged cycling life of Li-rich Mn-based oxides through spinel "lithium ion pump" heteroepitaxial coating strategy

Jili Li[a,*], Tiekun Jia[a,*], Chunjuan Tang[a], Dongsheng Yu[a,*], Jie Sun[a], Wanzhen Zhang[a], Yujiang Wang[a], Joong Hee Lee[b], Nam Hoon Kim[b]

[a] Material Science and Engineering School, Henan Province International Joint Laboratory of Materials for Solar Energy Conversion and Lithium Sodium based Battery & Henan Key Laboratory of Special Protective Materials, Luoyang Institute of Science and Technology, Luoyang 471023, China
[b] Department of Nano Convergence Engineering, Jeonbuk National University, Jeonju, Jeonbuk 54896, Republic of Korea

ARTICLE INFO

Article history:
Received 8 April 2021
Revised 15 June 2021
Accepted 30 June 2021
Available online 17 July 2021

Keywords:
Heteroepitaxial coating
Lithium-rich layered oxides
Voltage fading
Cathode

ABSTRACT

The practical application of Li-rich layered oxides is impeded by its cycle instability, poor rate capability and serious voltage decay. Here, nano-sized spinel $Li_4Ti_5O_{12}$ (LTO) is constructed on $Li_{1.2}Ni_{0.13}Co_{0.13}Mn_{0.54}O_2$ (LLNCMO). The distinctly heteroepitaxial structure of LTO nanocoating on LLNCMO is corroborated by HAADF-STEM. The LTO coating with fast lithium ion diffusion kinetics acts as "lithium ion pump" when Li^+-ions cross over it. The integrated structure can effectively retard oxygen evolution and phase transformation engendering higher capacity and voltage retention. LTO heteroepitaxially coated LLNCMO (LTO@LLNCMO) shows an improvement of initial coulombic efficiency to 74.3% and more stable life with a high capacity retention up to 96.9% at 2C after 500 cycles (40.5% for LLNCMO). LTO@LLNCMO demonstrates minimal voltage fading of 1.33 mV per cycle suggesting suppression of phase conversion to spinel-like structure. The epitaxial spinel modification strategy can be applied to control the surface stability of cathodes.

With the rapid expansion of portable electronics, electric vehicles and power grid, the existing lithium-ion batteries (LIBs) as an important power source urgently need to be ameliorated. [1,2] Especially, the insufficient energy-density of the cathode materials restricts their large-scale deployment. [3,4] Among the cathode materials studied, Li-rich layered oxides (LLOs) might surmount such limitations due to the redox reaction at higher voltage and a higher capacity surpassing 250 mAh g^{-1}. [5–9] Nonetheless, the large initial irreversible capacity loss, poor cycling stability, inferior rate capability and the voltage fading jeopardize the practical application of LLOs cathodes. [10–14] These issues might be caused by the irreversible structural rearrangement and phase transformation to spinel-like structure from surface to the interior. [15–17] Consequently, the improvement of surface structural stability might effectively raise the capacity and mitigate voltage fading for LLO cathodes.

It has been proved that surface coating is a simple and efficient remedy to reform the interfacial stability. [18–27] Although inert surface coatings, including some oxides, [18] fluorides [19] and phosphates [20,21] etc. can enhance the cyclic stability and power performance of LLOs partly, the lattice structures mismatch with the host LLO materials hardly creates a uniform safeguard and throughout integrated structure (or heteroepitaxial structure) during continuous cycling. Since spinel oxides have the same cubic close-packed oxygen arrays with LLOs, they can construct a coating with better structural compatibility throughout integrated structure. [23–29] Furthermore, a spinel structure with three-dimensional lithium diffusion tunnels can provide more active sites and faster diffusion kinetics for lithium ions. Therefore, some spinel oxides have been designed and built on the surface of LLOs to form an integrated structure leading to increase of the long cycling life, enhancement of rate capability and alleviation of voltage decay. Spinel $Li_4Mn_5O_{12}$ coating was constructed on the surface of $Li_{1.2}Mn_{0.54}Co_{0.13}Ni_{0.13}O_2$ material through the controlled $KMnO_4$ oxidation strategy. [29] The epitaxially $Li_4Mn_5O_{12}$-coated cathode displayed high cycling stability with a capacity retention of 83.1% and mitigated voltage decay of 0.525 V after 300 cycles at 0.2 C. There were other spinel structures on the surface of LLOs produced by chemical leaching reaction bringing about loss of lithium and non-uniform distribution of spinel structures.

* Corresponding authors.
E-mail addresses: lijili328@126.com (J. Li), tiekunjia@126.com (T. Jia), dongsh_yu@163.com (D. Yu).

https://doi.org/10.1016/j.scriptamat.2021.114133
1359-6462/

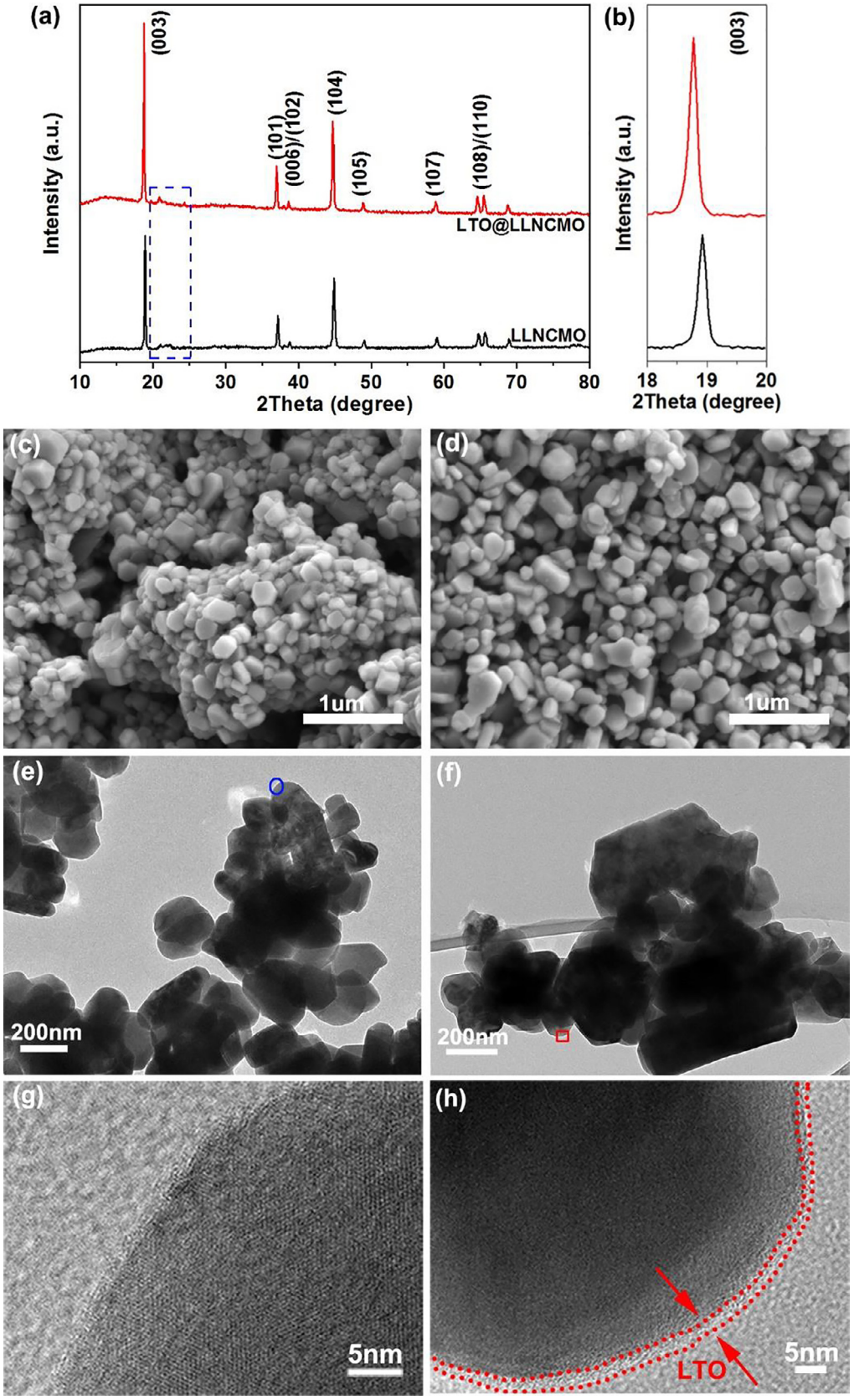

Fig. 1. Powder XRD patterns (a) and the (003) peaks (b) of LLNCMO and LTO@LLNCMO. SEM images of LLNCMO (c) and LTO@LLNCMO (d). TEM images of LLNCMO (e) and LTO@LLNCMO (f). HRTEM images of LLNCMO (g) and LTO@LLNCMO (h)

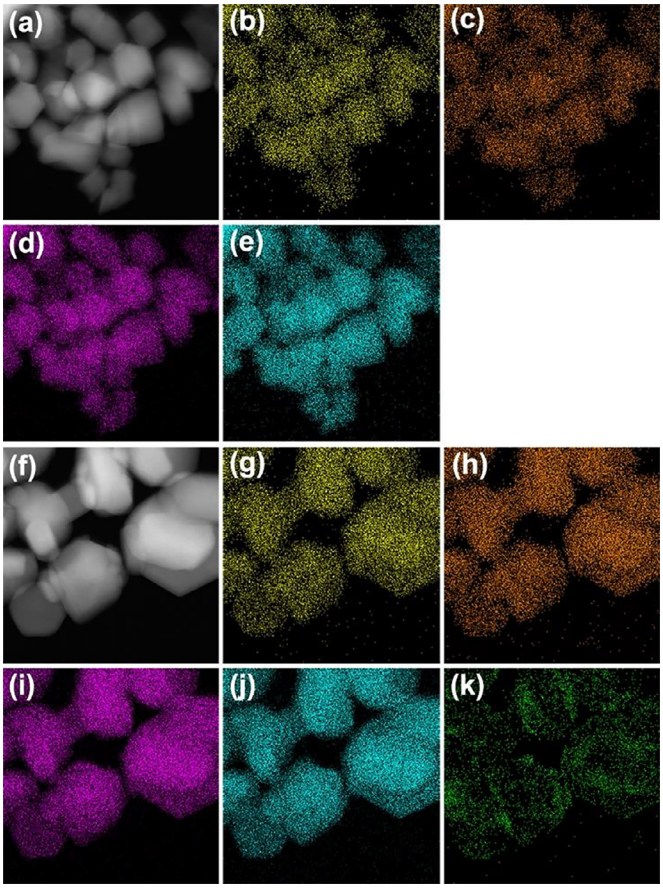

Fig. 2. HADDF-STEM images of LLNCMO (a) and LTO@LLNCMO (f) particles and the corresponding element mapping: (b, g) Ni, (c, h) Co, (d, i) Mn, (e, j) O, (k) Ti.

In animals and plants, there are some special carrier proteins called "Ion pump" which can drive specific ions such as Na^+, K^+, Ca^{2+} and H^+ across plasmolemma. Spinel $Li_4Ti_5O_{12}$ (LTO) with high Li^+ diffusion constant integrated on the surface of LLOs can speed transport of Li^+ ions between host material and electrolyte, [29] which acts as an ion pump called "lithium ion pump". The other merits of LTO including zero strain, 3D channels and no Jahn–Teller effect during lithiation/delithiation all reinforce the structural stability of LLOs. However, it is still a great challenge to develop a uniform spinel LTO coating on the whole surface of LLOs with heteroepitaxial structure.

In this paper, a heteroepitaxial composite of "lithium ion pump" LTO coated on $Li_{1.2}Ni_{0.13}Co_{0.13}Mn_{0.54}O_2$ (LLNCMO) was designed and synthesized. It is demonstrated that the nanoscale LTO coating with the integrated structure on the surface of LLNCMO can inhibit the surface oxygen activity and spinel-like phase transformation reaction, which leads to enhanced initial coulomb efficiency, superior cycling stability and high voltage retention. As a cathode for LIBs, the heteroepitaxial LTO coated LLNCMO (LTO@LLNCMO) material demonstrates enhancement of the initial coulombic efficiency (74.3 %), capacity retention (96.9 % at 2 C after 500 cycles) and mitigation of the voltage fading (1.33 mV $cycle^{-1}$). It illustrates that the heteroepitaxial LTO coating strategy can be applied to modify LLOs for fabricating high performance cathodes in next-generation LIBs.

X-ray diffraction (XRD) was carried out to investigate the structure of bare LLNCMO and LTO-coated LLNCMO materials, results are shown in Fig. 1a and b. All sharp reflections in the XRD patterns can be assigned to the layered α-$NaFeO_2$ structure (R-3m). The weak superlattice diffraction peaks between 20 and 25° can be ascribed to the monoclinic Li_2MnO_3 phase (C2/m space group). [30] After LTO coating, diffraction peaks for spinel LTO coating layer cannot be observed due to its low content. LTO@LLNCMO material still maintains the same structure with the bare Li-rich

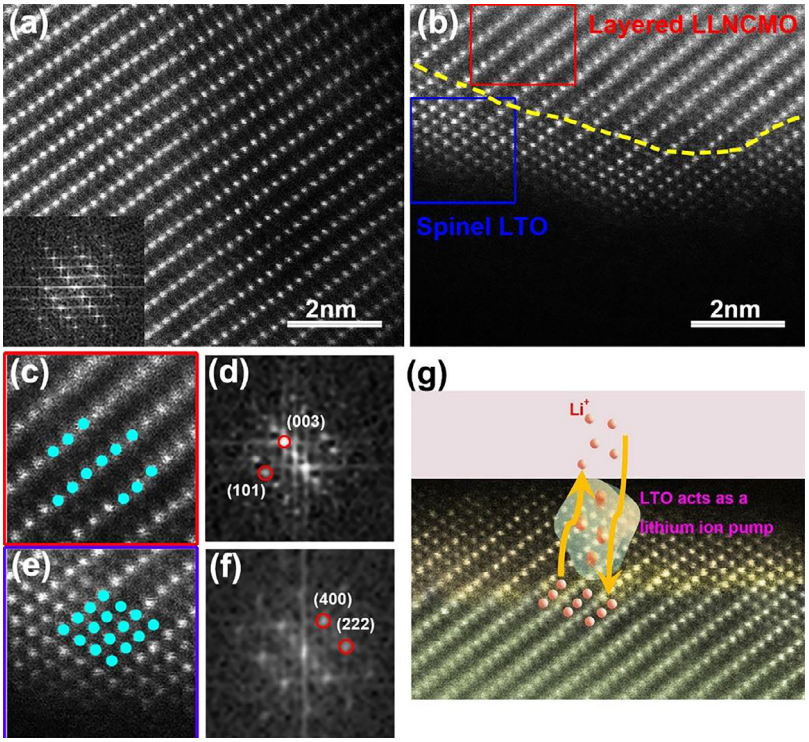

Fig. 3. (a) Atomic scale HAADF-STEM images of LLNCMO particles and the corresponding FFT pattern (the inset image). (b) Atomic scale HAADF-STEM image of LTO@LLNCMO sample; (c,d) the enlarged view of red region from (b) and the corresponding FFT pattern, which show the layered structure of LLNCMO; (e,f) the enlarged view of the coating layer (blue region from (b)) and the corresponding FFT pattern, which show the spinel structure of LTO. (g) The scheme of lithium ions through ultrathin LTO coating.

LLNCMO material. In the enlarged display of the (003) peaks (Fig. 1b), the peaks of the coated LTO@LLNCMO material obviously shifts to lower values illustrating the increase of *c* axis, which is beneficial for the Li-ion diffusion along the Li layer. [24]

The morphologies and microstructures of as-prepared materials were observed in SEM and TEM images to confirm the influence of LTO surface modification on the morphology, they are shown in Fig. 1c–h. SEM images demonstrate that the size of nanoparticles show no obvious variation after LTO surface modification, which is further proved by TEM. The only difference is that nanoparticles of LLNCMO material are aggregated together but LTO@LLNCMO nanoparticles have better dispersion, which is beneficial for the infiltration of electrolyte leading to superior electrochemical performance. It is clearly observed in the TEM images of LTO@LLNCMO materials that a uniform ultrathin LTO coating layer (Fig. 1h marked with red dotted lines) on the surface of LLNCMO nanoparticles with the thickness of approximately 2 nm has been formed. Elemental mappings of bare and LTO-coated LLNCMO materials shown in Fig. 2 were detected to illustrate the distribution of transition metal elements. In both bare LLNCMO and surface coated LTO@LLNCMO materials, nickel, cobalt and manganese are distributed uniformly with no segregation. Moreover, Ti is homogeneously distributed on the surface of nanoparticles for LTO@LLNCMO material. [31]

Atomic scale HAADF-STEM was used to clarify the surface and interface structures before and after LTO-coating LLNCMO materials, results are shown in Fig. 3. For bare LLNCMO material (Fig. 3a), it is demonstrated that the well crystallization extends from the inside to the surface of the nanoparticles with the identical *d*-spacing of 0.478 and 0.245 nm which can be assigned to (003) and (101) faces of LLNCMO, respectively. Furthermore, the surface structure of LTO@LLNCMO material is obviously different from that of LLNCMO. From the atomic scale HAADF-STEM images of LTO@LLNCMO material (Fig. 3b–f), the clear spinel LTO structure with a thickness of about 2 nm is found on the surface of layered LLNCMO nanoparticles and the two phases form an integrated structure in one nanoparticle, which has been referred to as heteroepitaxial structure due to the same oxygen arrays of layered LLNCMO and spinel LTO phases. [29,31,32] The interplanar distances of LTO coating are measured to be 0.244 and 0.238 nm corresponding to the (400) and (222) planes of spinel LTO structure, respectively. In addition, LTO surface spinel phase with excellent lithium ion transmission features can supply effective 3D diffusion routes for lithium ions which play a similar role to the ion pumps in animals and plants, as shown in Fig. 3g. LTO spinel phase on the surface of LLNCMO is expected to stabilize the structure, suppress irreversible oxygen release and voltage decay during Li^+-ion insertion/extraction leading to more outstanding electrochemical performance. [29,31]

XPS measurements were applied to characterize the surface compositions and chemical states of the transition metal ions and oxygen on the bare LLNCMO and LTO-coated LTO@LLNCMO materials, as shown in Figs. S1 and 4. Compared to the sum XPS pattern of as-prepared LLNCMO (Fig. S1a), there appear two new peaks at 455 ~ 468 eV for LTO@LLNCMO which can be assigned to the binding energy value of Ti2p. [28,30] It further testifies that spinel LTO is successfully constructed on the surface of LLNCMO nanoparticles. In the Ni2p and Co2p spectra in Fig. S1b and c, it can be found that the binding energy has no distinct variation before and after LTO coating and the chemical states of Ni and Co are +2 and +3, respectively. The peak locations of $Mn2p_{1/2}$ and $Mn2p_{3/2}$ are almost unchanged after LTO coated, which is further proved by the same level of Mn3s peak splitting (Figs. S1d and 4a). [27,29] The Mn3s peak splitting illustrates that the oxidation states of Mn ions in both LLNCMO and LTO@LLNCMO materials are slightly less than +4. This resulted from Mn^{2+} ions being oxidized insufficiently to

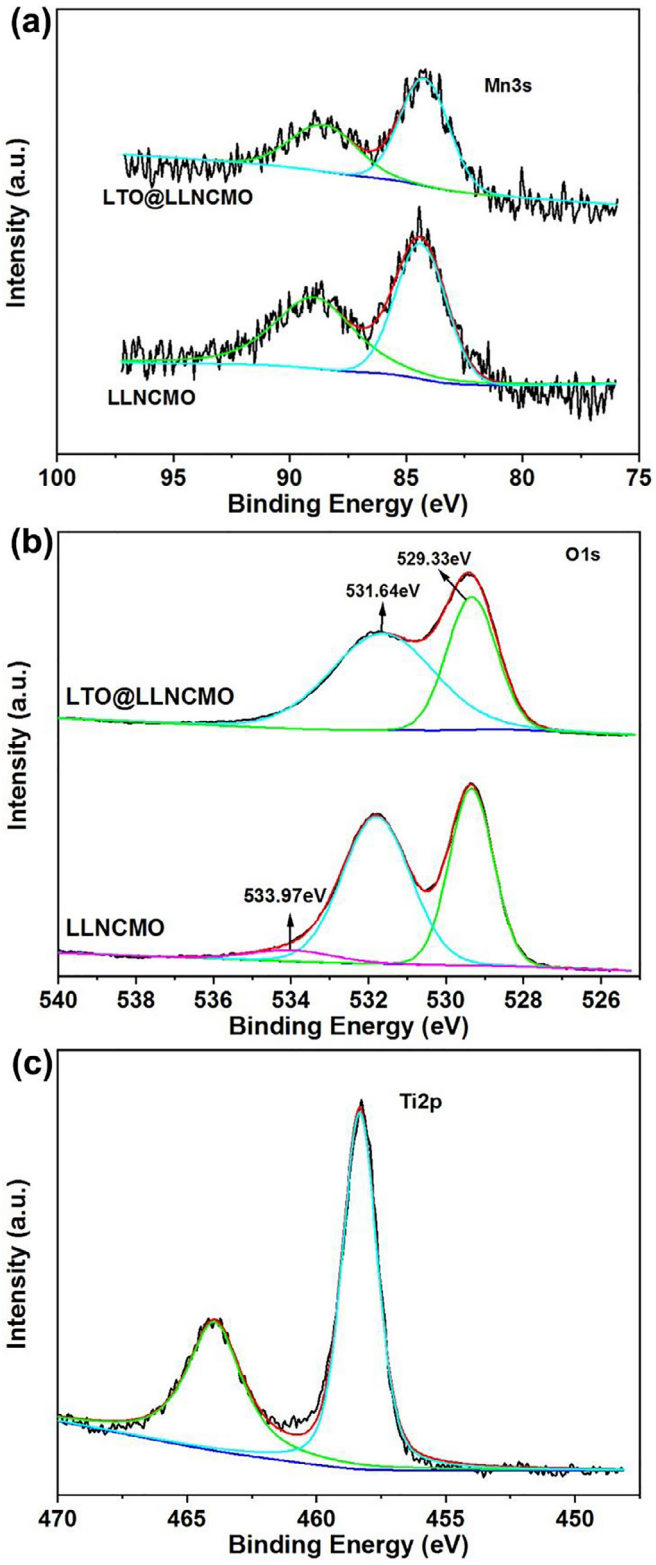

Fig. 4. XPS peaks of (a) Mn3s; (b) O1s; (c) Ti2p in LLNCMO and LTO@LLNCMO.

Mn^{4+} ions or oxygen vacancies are engendered in the synthetic process. [27] After LTO-modification, the average oxidation states of Mn ions in LTO@LLNCMO material still maintain about +3.77 with the same level in LLNCMO material. [27,28] The XPS of O1s in LTO@LLNCMO materials as shown in Fig. 4b still retain two peaks at 529.33 and 531.64 eV which belong to lattice oxygen in the

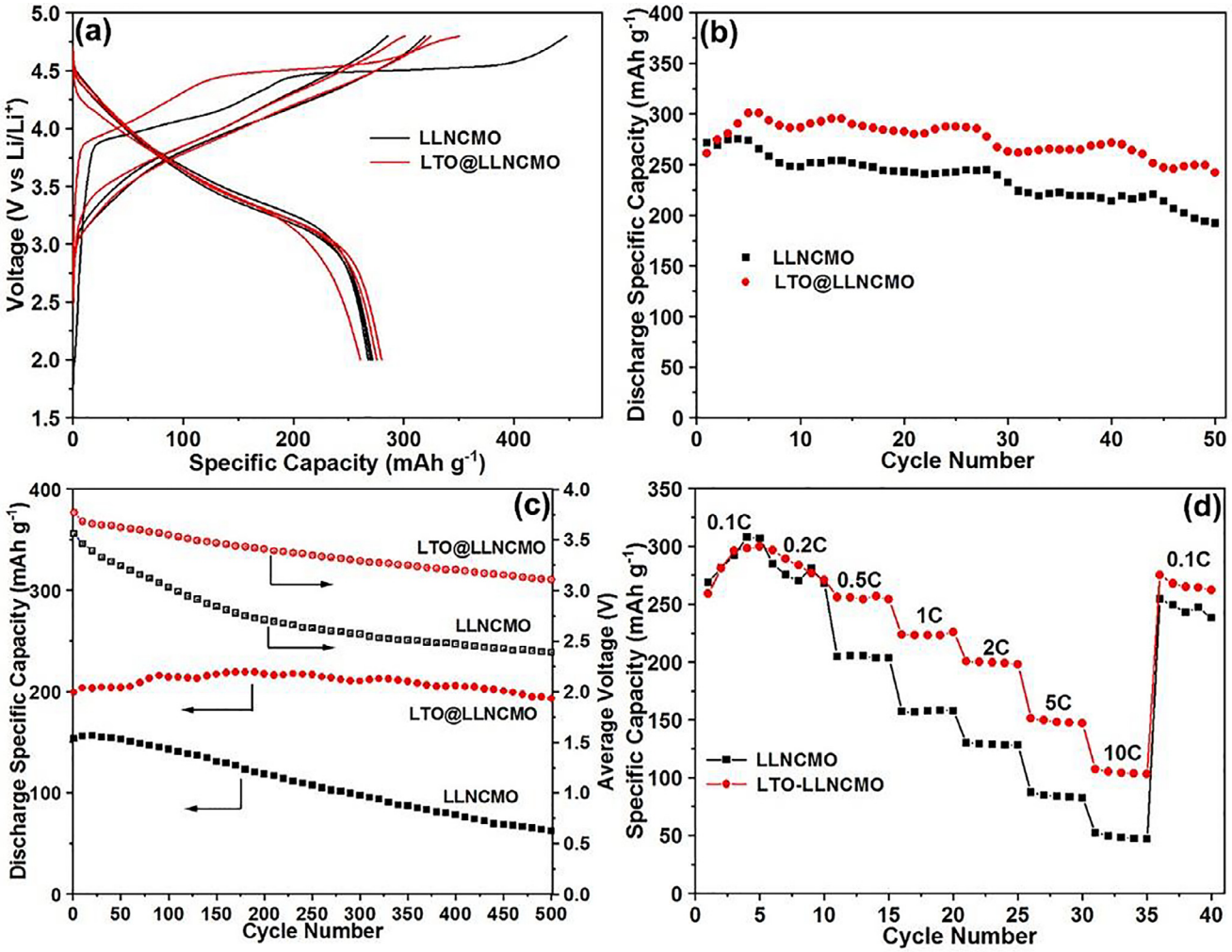

Fig. 5. The electrochemical performances of LLNCMO and LTO@LLNCMO cathodes: (a) the charge and discharge curves in the first three cycles at 0.1 C (1 C=200 mA g^{-1}); (b) the cycle life at 0.1 C; (c) the long term cycling at 2 C and the voltage fading, each point represents the average value of ten cycles; (d) the rate capability at different current densities.

crystal lattice and impurity lithium oxides on the surface of the layered cathode materials, respectively. [27,32] Compared to the O1s spectra in LLNCMO material, the peak at 533.97 eV disappears indicating more excellent surface stability in LTO coated material LTO@LLNCMO. From the Ti2p spectrum in LTO@LLNCMO material (Fig. 4c), the peaks at 458.33 and 463.94 eV can be attributed to $Ti2p_{3/2}$ and $Ti2p_{1/2}$ of Ti^{4+}.

Fig. 5 displays the electrochemical performance of LLNCMO materials before and after LTO heteroepitaxial coating. The first three charge and discharge curves at 0.1 C (1 C = 200 mA g^{-1}) are shown in Fig. 5a. For bare LLNCMO cathode, it demonstrates a high charge capacity up to 448.1 mAh g^{-1} and a discharge capacity of 271.7 mAh g^{-1} leading to a lower coulomb efficiency of 60.6 % in the initial cycle. LTO@LLNCMO cathode delivers the smaller first charge and discharge capacities of 350.8 and 260.6 mAh g^{-1}, respectively. Compared to the host LLNCMO cathode, the initial charge capacity of LTO heteroepitaxial coated cathode decreases more causing a larger coulomb efficiency of 74.3 %, which suggests that LTO heteroepitaxial coating layer could reduce the activity of oxygen in Li_2MnO_3 composition. [22] After 50 charge and discharge cycles at 0.1 C (Fig. 5b), the capacity of LLNCMO cathode dwindles to 192.2 mAh g^{-1} with a capacity retention of 70.7 %. After LTO heteroepitaxial modification, the capacity still retains 242.4 mAh g^{-1} corresponding to a progressive capacity retention up to 93.0 %. To examine the variation of cycling stability and the voltage decay of LLNCMO modified by ultrathin LTO heteroepitaxial coating layer at high current density, the charge and discharge of LLNCMO and LTO@LLNCMO cathodes are continued to 500 cycles at 2 C as shown in Fig. 5c. The discharge capacities are 153.5 and 199.3 mAh g^{-1} for LLNCMO and LTO@LLNCMO cathodes at 2 C, respectively, illustrating heightened lithium storage capacity at large current density. After 500 charge and discharge cycles, the discharge capacity of LLNCMO cathode rapidly deteriorates to 62.1 mAh g^{-1}. In contrast, LTO@LLNCMO cathode preserves high discharge capacity with a capacity retention of 96.9 % during 500 prolonged cycles, reflecting the benefits of the LTO heteroepitaxial coating layer on the structural stability. [30] Furthermore, the average discharge voltage of LLNCMO cathode quickly diminishes to 2.39 V in 500 charge and discharge cycles producing a strong voltage decay of 2.34 mV $cycle^{-1}$, much larger than 1.33 mV $cycle^{-1}$ for LTO@LLNCMO cathode. It demonstrates that LTO heteroepitaxial coating layer can effectively retard the structure transformation during repeated lithiation and delithiation, which is further certified by the TEM images after 50 cycles (Fig. S2). [27,29] The rate capabilities of LLNCMO and LTO@LLNCMO cathodes are also tested at different current densities, results are shown in Fig. 5d. The average discharge capacities are 286.7, 283.4, 255.4, 223.8, 199.3, 148.7 and 104.7 mAh g^{-1} at 0.1, 0.2, 0.5, 1, 2, 5 and 10 C for LTO@LLNCMO cathode,

respectively. Except for at 0.1 C, the average discharge capacities of the LTO-coated cathode are all enhanced at every current density. Specifically, the average discharge capacity of LTO@LLNCMO cathode is 104.7 mAh g^{-1} at 10 C considerably higher than that of LLNCMO cathode. Compared with the electrochemical performance of bare LLNCMO cathode, LTO@LLNCMO evinces impressively optimum long cycle life and the charge/discharge ability at large current density due to the distinctive surface and interface structure. The integrated structure of LTO spinel heteroepitaxial coating layer and host LLNCMO guarantees the super stability and smoother channels for Li^+ ions insertion/extraction. In addition, ultrathin LTO with 3-dimensional diffusion path can further improve the kinetic process of lithium ion diffusion without reducing the electronic conductivity.

To further understand the redox process, cyclic voltammetry (CV) was done between 2.0 and 4.8 V with 0.1 mV s^{-1} (Fig. S3). The redox peaks of LLNCMO and LTO@LLNCMO cathodes both are consistent with the reported $Li_{1.2}Ni_{0.13}Co_{0.13}Mn_{0.54}O_2$ system in the literatures. [29–31] The anodic peaks above 4.5 V can be assigned to the extraction of lithium from Li_2MnO_3 accompanied by oxygen release. [13] Another broad anodic peaks at about 4.1 V corresponds to the oxidation of the transition metal ions Ni^{2+} and Co^{3+}. [13,33] The cathodic peaks located at approximately 3.7 V belong to the reduction of the transition metal ions. The anodic peaks shift to lower potential and the cathodic peak shifts to higher potential for LTO@LLNCMO cathode compared with the bare LLNCMO, which suggests the improved reversibility of redox reaction after ultrathin LTO coated.

The kinetics of electrochemical reaction in LLNCMO and LTO@LLNCMO cathodes can be surveyed by electrochemical impedance spectroscopy. The Nyquist plots before and after 50 cycles at 0.1 C fitted with equivalent circuit (Fig. S4–S6) are all composed of a semicircle and a sloped line, which are the impedance of the solid electrolyte interface (R_{SEI}) and the charge transfer resistance (R_{ct}) and the Warburg resistance (W) reflecting the lithium-ion diffusion process in the solid electrode, respectively. [34–37] Before cycling, the resistance of R_{SEI} and R_{ct} displays 232.0 Ω for LTO@LLNCMO cathode, which is much smaller than 625.2 Ω for bare LLNCMO cathode. It illustrates that LTO can boost the charge transfer reaction. Although the values of R_{SEI} and R_{ct} of the two cathodes are both abated after 50 charge/discharge cycles, LTO@LLNCMO cathode still manifests a lower resistance than that of LLNCMO cathode. This implies that the formation of stronger SEI film on the surface of ultrathin LTO heteroepitaxial coating layer with prominent rate capability.

In summary, we designed a spinel $Li_4Ti_5O_{12}$ nano-sized coating on the surface of $Li_{1.2}Ni_{0.13}Co_{0.13}Mn_{0.54}O_2$ material to alleviate the inferior electrochemical performances, especially serious voltage loss. The heteroepitaxial structure is formed between nano-sized LTO coating and LLNCMO material because of the compatibility of the lattice structures. As cathode for LIBs, LTO heteroepitaxially coated LLNCMO (LTO@LLNCMO) cathode displays higher initial coulombic efficiency of 74.3 % than that of 60.6 % for LLNCMO cathode. The cycle stability is also enhanced up to 96.9 % capacity retention at 2 C after 500 cycles (40.5 % for LLNCMO). Moreover, the voltage decay is reduced from 2.34 to 1.33 mV $cycle^{-1}$ after coating with spinel LTO. The excellent electrochemical properties indicate that the epitaxial LTO coating could restrain the surface phase transformation into spinel-like structure for LLNCMO material. In addition, spinel LTO coating with 3D lithium ion diffusion channels and more prominent lithium ion diffusion kinetics can drive Li^+ ions quickly across the interface of LLNCMO and electrolyte acting as “lithium ion pump”. This spinel LTO heteroepitaxially coated strategy can be extended to modify other LLOs for high performance next-generation LIBs.

Declaration of Competing Interest

The authors declare that they have no known competing financial interests or personal relationships that could have appeared to influence the work reported in this paper.

Acknowledgement

This work was supported by the National Natural Science Foundation of China (51702148, 51802139), Henan Science and Technology Research Program (182102410074, 172102410047) and the Training Plan of Young Backbone Teachers in Colleges and Universities of Henan Province (2019GGJS244, 2018GGJS156) .

Supplementary materials

Supplementary material associated with this article can be found, in the online version, at doi:10.1016/j.scriptamat.2021.114133.

References

[1] D. Larcher, J.M. Tarascon, Nat. Chem. 7 (2014) 19–29.
[2] M. Li, J. Lu, Z. Chen, K. Amine, Adv. Mater. 30 (2018) 1800561.
[3] J. Wu, Y. Cao, H. Zhao, J. Mao, Z. Guo, Carbon Energy 1 (2019) 57–76.
[4] H. Liu, H. Guo, B. Liu, M. Liang, Z. Lv, K.R. Adair, X. Sun, Adv. Funct. Mater. 28 (2018) 1707480.
[5] Z. Lu, D.D. MacNeil, J.R. Dahn, Electrochem. Solid-State Lett. 4 (2001) A191–A194.
[6] G. Assat, J.-M. Tarascon, Nat. Energy 3 (2018) 373–386.
[7] W.E. Gent, K. Lim, Y. Liang, Q. Li, T. Barnes, S.J. Ahn, K.H. Stone, M. McIntire, J. Hong, J.H. Song, Y. Li, A. Mehta, S. Ermon, T. Tyliszczak, D. Kilcoyne, D. Vine, J.H. Park, S.K. Doo, M.F. Toney, W. Yang, D. Prendergast, W.C. Chueh, Nat. Commun. 8 (2017) 2091.
[8] J.L. Shi, D.D. Xiao, M. Ge, X. Yu, Y. Chu, X. Huang, X.D. Zhang, Y.X. Yin, X.Q. Yang, Y.G. Guo, L. Gu, L.J. Wan, Adv. Mater. 30 (2018) 1705575.
[9] Y. Shen, H. Xue, S. Wang, D. Zhang, D. Yin, L. Wang, Y. Cheng, Chem. Eng. J. 411 (2021) 128487.
[10] J.C. Zhang, F.Y. Cheng, S.L. Chou, J.L. Wang, L. Gu, H. Wang, H. Yoshikawa, Y. Lu, J. Chen, Adv. Mater. 31 (2019) 1901808.
[11] M. Sathiya, A.M. Abakumov, D. Foix, G. Rousse, K. Ramesha, M. Saubanère, M.L. Doublet, H. Vezin, C.P. Laisa, A.S. Prakash1, D. Gonbeau, G. VanTendeloo, J.-M. Tarascon, Nat. Mater. 14 (2014) 230–238.
[12] J. Lee, Q. Zhang, J. Kim, N. Dupre, M. Avdeev, M. Jeong, W.-S. Yoon, L. Gu, B. Kang, Adv. Energy Mater. 9 (2019) 1902231.
[13] T. Lin, T.U. Schulli, Y. Hu, X. Zhu, Q. Gu, B. Luo, B. Cowie, L. Wang, Adv. Funct. Mater. 30 (2020) 1909192.
[14] J. Lee, Y. Gong, L. Gu, B. Kang, ACS Energy Lett. 6 (2021) 789–798.
[15] N. Li, S. Hwang, M. Sun, Y. Fu, V.S. Battaglia, D. Su, W. Tong, Adv. Energy Mater. 9 (2019) 1902258.
[16] S. Sharifi-Asl, V. Yurkiv, A. Gutierrez, M. Cheng, M. Balasubramanian, F. Mashayek, J.R Croy, R. Shahbazian-Yassar, Nano Lett. 20 (2020) 1208–1217.
[17] W. Hua, S. Wang, M. Knapp, S.J. Leake, A. Senyshyn, C. Richter, M. Yavu, J.R. Binder, C.P. Grey, H. Ehrenberg, S. Indris, B. Schwarz, Nat. Commun. 10 (2019) 5365.
[18] B. Qiu, M. Zhang, L. Wu, J. Wang, Y. Xia, D. Qian, H. Liu, S. Hy, Y. Chen, K. An, Y. Zhu, Z. Liu, Y.S. Meng, Nat. Commun. 7 (2016) 12108.
[19] X. Zhang, I. Belharouak, L. Li, Y. Lei, J.W. Elam, A. Nie, X. Chen, R.S. Yassar, R.L. Axelbaum, Adv. Energy Mater. 3 (2013) 1299–1307.
[20] T. Zhao, L. Li, R. Chen, H. Wu, X. Zhang, S. Chen, M. Xie, F. Wu, J. Lu, K. Amine, Nano Energy 15 (2015) 164–176.
[21] R. Yu, M.N. Banis, C. Wang, B. Wu, Y. Huang, S. Cao, J. Li, S. Jamil, X. Lin, F. Zhao, W. Lin, B. Chang, X. Yang, H. Huang, X. Wang, X. Sun, Energy Storage Mater. 37 (2021) 509–520.
[22] J. Yang, P. Li, F. Zhong, X. Feng, W. Chen, X. Ai, H. Yang, D. Xia, Y. Cao, Adv. Energy Mater. 10 (2020) 1904264.
[23] F. Zheng, C. Yang, X. Xiong, J. Xiong, R. Hu, Y. Chen, M. Liu, Angew. Chem. Int. Ed. 54 (2015) 13058–13062.
[24] Y. Wang, L. Wang, X. Guo, T. Wu, Y. Yang, B. Wang, E. Wang, H. Yu, ACS Appl. Mater. Interfaces 12 (2020) 8306–8315.
[25] D. Luo, G. Li, C. Fu, J. Zheng, J. Fan, Q. Li, L. Li, Adv. Energy Mater. 4 (2014) 1400062.
[26] H. Liu, C. Du, G. Yin, B. Song, P. Zuo, X. Cheng, Y. Ma, Y. Gao, J. Mater. Chem. A 2 (2014) 15640–15646.
[27] X.K. Ding, D. Luo, J.X. Cui, H.X. Xie, Q.Q. Ren, Z. Lin, Angew. Chem. Int. Ed. 59 (2020) 7778–7782.
[28] D. Luo, J. Cui, B. Zhang, J. Fan, P. Liu, X. Ding, H. Xie, Z. Zhang, J. Guo, F. Pan, Z. Lin, Adv. Funct. Mater. 31 (2021) 2009310.
[29] X.-D. Zhang, J.-L. Shi, J.-Y. Liang, Y.-X. Yin, J.-N. Zhang, X.-Q. Yu, Y.-G. Guo, Adv. Mater. 30 (2018) 1801751.

[30] J. Li, T. Jia, K. Liu, J. Zhao, J. Chen, C. Cao, J. Power Sources 333 (2016) 37–42.
[31] J. Li, Y. Zhu, L. Wang, C. Cao, ACS Appl. Mater. Interfaces 6 (2014) 18742–18750.
[32] Z. Lin, D. Luo, X. Ding, J. Fan, Z. Zhang, P. Liu, X. Yang, J. Guo, S. Sun, Angew. Chem. Int. Ed. 59 (2020) 23061–23066.
[33] W. Hua, M. Chen, B. Schwarz, M. Knapp, M. Bruns, J. Barthel, X. Yang, F. Sigel, R. Azmi, A. Senyshyn, A. Missiul, L. Simonelli, M. Etter, S. Wang, X. Mu, A. Fiedler, J.R. Binder, X. Guo, S. Chou, B. Zhong, S. Indris, H. Ehrenberg, Adv. Energy Mater. 9 (2019) 1803094.
[34] N. Wu, H. Wu, J.-K. Kim, X. Liu, Y. Zhang, ChemElectroChem, 5 (2018) 78–83.
[35] N. Wu, X. Qiao, J. Shen, G. Liu, T. Sun, H. Wu, H. Hou, X. Liu, Y. Zhang, X. Ji, Electrochim. Acta 299 (2019) 540–548.
[36] C. Xu, J. Li, X. Feng, J. Zhao, C. Tang, B. Ji, J. Hu, C. Cao, Y. Zhu, F.K. Butt, Electrochim. Acta 358 (2020) 136901.
[37] N. Wu, J. Shen, L. Sun, M. Yuan, Y. Shao, J. Ma, G. Liu, D. Guo, X. Liu, Y.-B. He, Electrochim. Acta 310 (2019) 70–77.